Photonics and Nanostructures - Fundamentals and Applications 48 (2022) 100986

Contents lists available at ScienceDirect

Photonics and Nanostructures - Fundamentals and Applications

journal homepage: www.elsevier.com/locate/photonics

# Multi-octave supercontinuum generation in $As_2Se_3$ chalcogenide photonic crystal fiber

Lanh Chu Van [a], Thuy Nguyen Thi [b], Bao Tran Le Tran [a], Duc Hoang Trong [b], Ngoc Vo Thi Minh [a,c], Hieu Van Le [d], Van Thuy Hoang [a,*]

[a] Department of Physics, Vinh University, 182 Le Duan, Vinh, Viet Nam
[b] Hue University of Education, Hue University, 34 Le Loi Street, Hue, Viet Nam
[c] Huynh Thuc Khang High School, La Grai district, Gia Lai, Viet Nam
[d] Faculty of Natural Sciences, Hong Duc University, 565 Quang Trung Street, Thanh Hoa, Viet Nam

ARTICLE INFO

*Keywords:*
Photonic crystal fiber
Supercontinuum generation
Dispersion
Nonlinear optics
Coherence

ABSTRACT

We numerically calculated multi-octave spanning supercontinuum generation (SCG) in two proposed $As_2Se_3$ photonic crystal fibers (PCFs) with low input peak powers and highly coherent characteristics with the effects of vacuum noise and pulse-to-pulse relative intensity noise. The first PCF with a lattice constant ($\Lambda$) of 1.5 μm and core diameter ($d_{core}$) of 5.48 μm has the flat all-normal dispersion in the wavelength range of 2–10 μm. For the input peak power of 5 kW, this fiber generates the all-normal dispersion SCG with a spectral bandwidth of 1.85–5.7 μm with pump wavelength at 3.5 μm, and two octave-spanning of 1.9–7.6 μm with pump wavelength at 5.5 μm. The second PCF with $\Lambda$ of 1.52 μm and $d_{core}$ of 7.3 μm has flat dispersion and two zero-dispersion wavelengths at 4.3 μm and 7.8 μm. By launching the input peak power of 7.5 kW, and pump wavelength at 3.5 μm, the second PCF generates the broad SCG with a spectral bandwidth of 2–10 μm. The SCG in two proposed PCFs has high coherence due to the effects of vacuum noise. However, the results of our works point out that pulse-to-pulse relative intensity noise significantly decreases the coherence. The amount of coherence reduction depends on the pulse duration and the physical mechanism for spectral broadening in which a part of the supercontinuum spectrum induced by optical wave breaking and dispersive wave experiences a remarkable reduction of coherence due to the effects of pulse-to-pulse relative intensity noise.

## 1. Introduction

Fiber-based supercontinuum (SC) sources with broad spectral bandwidth and high brightness have found widespread applications in optical coherence tomography [1,2] frequency metrology [3,4] fluorescence lifetime imaging [5]. Recently, the SC sources cover the spectrum from ultraviolet (UV) up to the mid-infrared (IR) range with the brightness 1–2 orders higher than that of a typical synchrotron beamline [6]. They are also recognized and well-established technology with plenty of solutions, including commercial ones. The general approach for supercontinuum generation (SCG) is to launch the laser pulses with high peak power into a nonlinear optical fiber. Due to the effects of dispersion and nonlinearity, the input pulses are broadened in both temporal and spectral profiles [7]. The nonlinear fibers are typically fabricated from silica because this material has high transparency, exceptional purity, non-crystallization, and easy for fiber fabrication using the conventional stack-and-draw method. However, the main drawback of silica, besides the low nonlinearity, is a limitation of transmission in IR range. Therefore, SC sources based on the silica fiber are typically limited to around 2.4 μm.

The development of non-silica materials with high nonlinearity and high transparency in the IR range has been bringing the SCG with a spectral bandwidth that exceeds the inherent limitation of silica. Chemnitz et. al. reported the SCG (up to 3 μm) induced by hybrid soliton dynamics in liquid-core fiber [8]. The hybrid soliton originates from the non-instantaneous mechanism, and it can mitigate the effects of vacuum noise. As a result, soliton-induced SCG in the liquid core fibers exhibits a high coherence across the entire generated bandwidth [8]. With the high nonlinearity and high transparency of selected liquids, liquid-core fibers enable the broad SCG from visible to mid-IR range with low input peak powers [9–12]. Other works considered antiresonant fibers infiltrated with noble gases for SCG. The gas-core fibers, with the flexibility to

* Corresponding author.
*E-mail address:* thuyhv@vinhuni.edu.vn (V.T. Hoang).

https://doi.org/10.1016/j.photonics.2021.100986
Received 20 April 2021; Received in revised form 24 October 2021; Accepted 15 December 2021
Available online 17 December 2021

optimize the dispersion and nonlinearity via changing the pressure and temperature, have been used for broad SCG ranging from UV to mid-IR range [13,14]. However, the use of liquid core and gas core fibers usually needs an additional system, such as a liquid reservoir or gas cell, to keep the liquid/gas fully into the core during the SCG measurements [13–15]. Moreover, the free-space coupling is necessary for the SCG system because the coupling of liquid-core/gas core fibers with standard silica fibers is still a challenge. Therefore, the development of a compact all-fiber SCG system with the use of liquid-core/gas core fibers is limited.

Another attractive approach for SCG is to use optical fibers made from soft glasses, such as telluride [16], ZBLAN [17], chalcogenide [17–20]. Among the soft glasses, chalcogenide glasses have a high nonlinear refractive index and high transparency from visible to mid-IR range, even up to 20 μm [17,19]. The SCG in chalcogenide fibers have covered the biological and chemical "fingerprint" region of the electromagnetic spectrum, and it is the potential to use for applications in microscopy [21], spectroscopy [22], biomedical imaging [23], and early cancer diagnostics [24].

A number of several experimental and theoretical investigations on mid-IR SCG have been demonstrated in chalcogenide fibers [17,19]. Due to the straightforward fiber fabrication, the step-index chalcogenide fibers are used for SCG up to 16 μm [25]. However, the step-index fibers have the limitation of design to optimize the dispersion and mode properties for SCG. In such a case, the dispersion of the fibers is modified by only changing the core diameter or fiber materials. Other methods to modify the properties of step-index fibers have been reported in [26–29]. The post-processing method using tapered chalcogenide fibers can offer the fibers with small effective mode areas and all-normal dispersion in the investigated wavelength range [26,27]. Other works used the cascade fibers systems for SCG with a commercial femtosecond laser as a pump source [28,29]. In this system, the laser pulse is coupled into the fiber with a zero-dispersion wavelength (ZDW) closed to the pump wavelength, the laser pulse is broadened, and then, coupled into the chalcogenide fiber to extremely spans the pulse up to mid-IR range.

As an alternative, chalcogenide photonic crystal fibers (PCFs) with the design flexibility to modify the fiber dispersion characteristics have been considered for SCG. In the case of PCFs, the dispersion and mode properties can be optimized by changing the geometrical parameters,.i.e, lattice pitch, size of air holes in the cladding region. The selection of previous works for broad-spanning SCG (more than one octave) in chalcogenide PCFs is shown in Table 1. The PCF with the size of air holes in the first ring smaller than that of outer rings in the cladding region offers the all-normal SCG with a spectral bandwidth of 2–4.55 μm [30]. The further decrease of core diameters increases the nonlinear coefficients, and thus, the PCF with a core diameter of around 1.3 μm generates the all-normal dispersion SCG with a spectral bandwidth of 2–9 μm with low input peak power (1.6 kW) [31]. The circle lattice PCF with a core diameter of 3.2 μm is also used for the all-normal dispersion SCG with a spectral bandwidth of 1.6–7 μm [39]. PCFs with the difference of material between the core, rod in the cladding, and the substrate are considered for SCG [33,41]. The modification of the material of cladding holes leads to the change in the contrast of refractive index between the core and cladding, and thus, this can optimize the dispersion and mode properties of the fibers for SCG. The $As_2S_5$-based PCF, with the first ring of hole-cladding made from borosilicate, has the flat all-normal dispersion from near to mid-IR range [33], and it is impossible to use further short pump wavelength (2.5 μm) for broad all-normal dispersion SCG with a spectral bandwidth of 1.05 – 5.05 μm [33]. Other works consider the chalcogenide PCFs for anomalous dispersion SCG [32,34–36,40]. The soliton dynamics are the dominant contribution for broad spectral broadening with low input peak power. However, the soliton-induced SC spectrum is not flat and exhibits low coherence via the effects of vacuum noise.

Almost all of the previous works use the chalcogenide PCF with a small core diameter (below 4.5 μm) [30–33,35–40] for mid-IR SCG. Unfortunately, the small core PCF typically has high confinement loss in the long-wavelength range, this leads to the reduction of spectral broadening and brightness of the SCG at the long wavelength. Moreover, the small core fiber offers a low coupling efficiency of the light from the laser into the fiber core in SCG measurement. Besides, all of the previous works considered only the effects of vacuum noise on the coherence of the SCG. It is worth noting that the coherence also depends on the other noise, e.g, pulse-to-pulse relative intensity noise (pulse-to-pulse noise) [42]. Therefore, taking pulse-to-pulse noise into account the analysis of the coherence of SCG is necessary.

In this paper, optical properties of solid core $As_2Se_3$-based photonic crystal fibers with various lattice constant $\Lambda$ and filling factor $d/\Lambda$ are numerically investigated in the mid-IR range. Chromatic dispersion and linear properties have been thoroughly analyzed by taking into account the effects of the lattice constant $\Lambda$ and the filling factor $d/\Lambda$. The values of $\Lambda$ and $d/\Lambda$ vary in the range of 1–2.5 μm, and 0.3–0.8, respectively. Next, the SCG in two proposed PCFs with flat dispersion is simulated using femtosecond laser pulses. The coherence of SCG with the effects of vacuum noise and pulse-to-pulse noise is also numerically calculated. We chose $As_2Se_3$ because this glass has a high nonlinear refractive index of $1.1 \times 10^{-17}$ $m^2$ $W^{-1}$ [43] and high transparency. The softening temperature of the $As_2Se_3$ glass is around 188 °C that allows coating the final fiber structure with other materials such as Poly (methyl methacrylate) during the fiber fabrication process.

## 2. Numerical modeling

The schematic cross-section geometrical structure of the solid core $As_2Se_3$ based PCF is shown in Fig. 1. The fiber structure is in a hexagonal lattice with seven rings in the air-holes cladding region. The light is propagated in the defect of the fiber structure by removing two central rings of air-holes. The core diameter is determined by the formula $d_{core} = 4\Lambda - d$, where $\Lambda$ and $d$ are lattice constant and the diameter of the air

**Table 1**
The SCG in chalcogenide PCFs with broad spectral bandwidth (more than one octave) pumped by femtosecond pulses.

| # | ChG glass | Pump wavelength (μm) | Pulse duration (fs) | Peak power (kW) | Spectral bandwidth (μm) | Normal/anomalous dispersion | Refs | Year. Pub |
|---|---|---|---|---|---|---|---|---|
| 1 | $As_2S_3$ | 3 | 50 | 1 | 2–4.55 | all-normal | [30] | 2013 |
| 2 | $As_2Se_3$ | 5.24 | 50 | 1.6 | 2–9 | all-normal | [31] | 2015 |
| 3 | $Ge_{11.5}As_{24}Se_{64.5}$ | 3.1 | 85 | 3 | 1–15 | anomalous | [32] | 2016 |
| 4 | $As_2S_5$ | 2.5 | 50 | 28.16 | 1.05–5.05 | all-normal | [33] | 2016 |
| 5 | $Ge_{11.5}As_{24}Se_{64.5}$ | 4.1 | 50 | 2 | 2–15 | anomalous | [34] | 2017 |
| 6 | $As_2S_3$ | 2.5 | 100 | 20 | 1–10 | anomalous | [35] | 2018 |
| 7 | $Ga_8Sb_{32}S_{60}$ | 4 | 90 | 8.19 | 1–14 | anomalous | [36] | 2018 |
| 8 | $As_{39}Se_{61}$ | 3.35 | 50 | 5 | 1.95–6.58 | all-normal | [37] | 2019 |
| 9 | $Ga_8Sb_{32}S_{60}$ | 4.5 | 50 | 20 | 1.65–9.24 | all-normal | [38] | 2019 |
| 10 | $Ge_{15}Sb_{15}Se_{70}$ | 3 | 50 | 20 | 1.6–7 | all-normal | [39] | 2019 |
| 11 | $GeSe_2As_2Se_3PbSe$ | 3 | 85 | 0.95 | 2–11 | anomalous | [40] | 2020 |
| 12 | $As_2Se_3$, $AsSe_2$ and $As_2S_5$ | 5 | 200 | 20 | 2.2–10 | all-normal | [41] | 2020 |

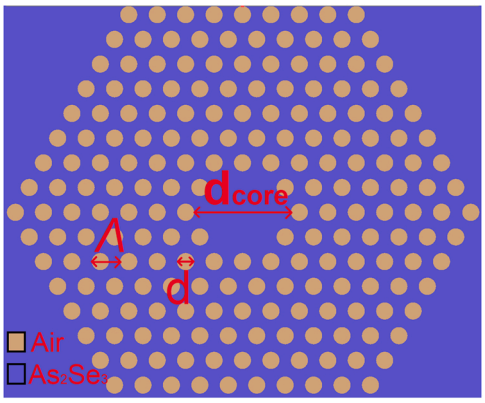


**Fig. 1.** The geometrical structures of large solid core PCFs with hexagonal and $As_2Se_3$ substrate.

holes, respectively.

The refractive index of $As_2Se_3$ is shown in Sellmeier's equation as given in Eq. (1) [44]:

$$n^2 - 1 = \frac{4.994872\lambda^2}{\lambda^2 - 0.24164^2} + \frac{0.120715\lambda^2}{\lambda^2 - 19^2} + \frac{1.712369\lambda^2}{\lambda^2 - 4 \times 0.24164^2} \quad (1)$$

The fiber dispersion consists of the waveguide and material dispersion. It is determined as given in Eq. (2), where Re[$n_{eff}$] is the real part of the effective refractive index of a guided mode.

$$D = -\frac{\lambda}{c}\frac{d^2\left(Re\left[n_{eff}\right]\right)}{d\lambda^2} \quad (2)$$

The preliminary simulation for dispersion with different values of lattice constant and diameter of air-holes is implemented using the finite difference eigenmode (FDE) method with a commercial Lumerical Model Solution [45]. In the case of the FDE method, the cross-section of fiber is divided into many rectangular sections. Each section has a size of 80 nm. In simulations, the lattice constant varies from 1.0 to 2.5 μm and the filling factor $d/\Lambda$ varies from 0.3 to 0.85. The boundary condition for the simulation herein is perfect matched layer (PML) boundaries. This boundary condition allows the radiation to propagate out of the computational area without an interferometer with the field inside, and boundaries absorb incident light upon them.

Fiber dispersion characteristics with various values of lattice constant and filling factors are presented in Fig. 2. In the case of small cores ($\Lambda = 1$ and 1.5 μm), the dispersion shapes critically depend on $\Lambda$ and $d/\Lambda$ (i.e., increase of $d/\Lambda$ leads to the dispersion that is clearly shifted toward the anomalous regime). In contrast, the fibers with further large cores ($\Lambda = 2.5$ μm) have dispersion shapes which are not sensitive to changing of $\Lambda$ and $d/\Lambda$.

Almost all of the investigated PCFs have two ZDWs, Fig. 2. The short zero-dispersion wavelengths ($ZDW_1$) are located around 3–4 μm, and the other one ($ZDW_2$) is from mid-IR to long-wavelength IR range. For a given value of $\Lambda$, the increase of the filling factor leads to the blueshifts of $ZDW_1$ while $ZDW_2$ shifts toward longer wavelengths.

Due to the negative effects of the material dispersion of $As_2Se_3$, the large core fibers have anomalous dispersion in the mid-IR range with $\lambda > 5$ μm, Fig. 2(c,d). Meanwhile, the fibers with a small value of $\Lambda$ offer the all-normal dispersion with the value of filling factor below 0.45. For a given value of $\Lambda$, the dispersion is shifted toward the normal regime with the decrease of the filling factor. Especially, with $\Lambda = 1$ and 1.5 μm, the dispersion is completely located in the normal dispersion with a small value of the filling factor.

Since dispersion is one of the significant factors for the SCG, the fiber with flat dispersion allows obtaining further broad SCG. Thus, the goal of optimization of dispersion herein is to show the fiber structures with

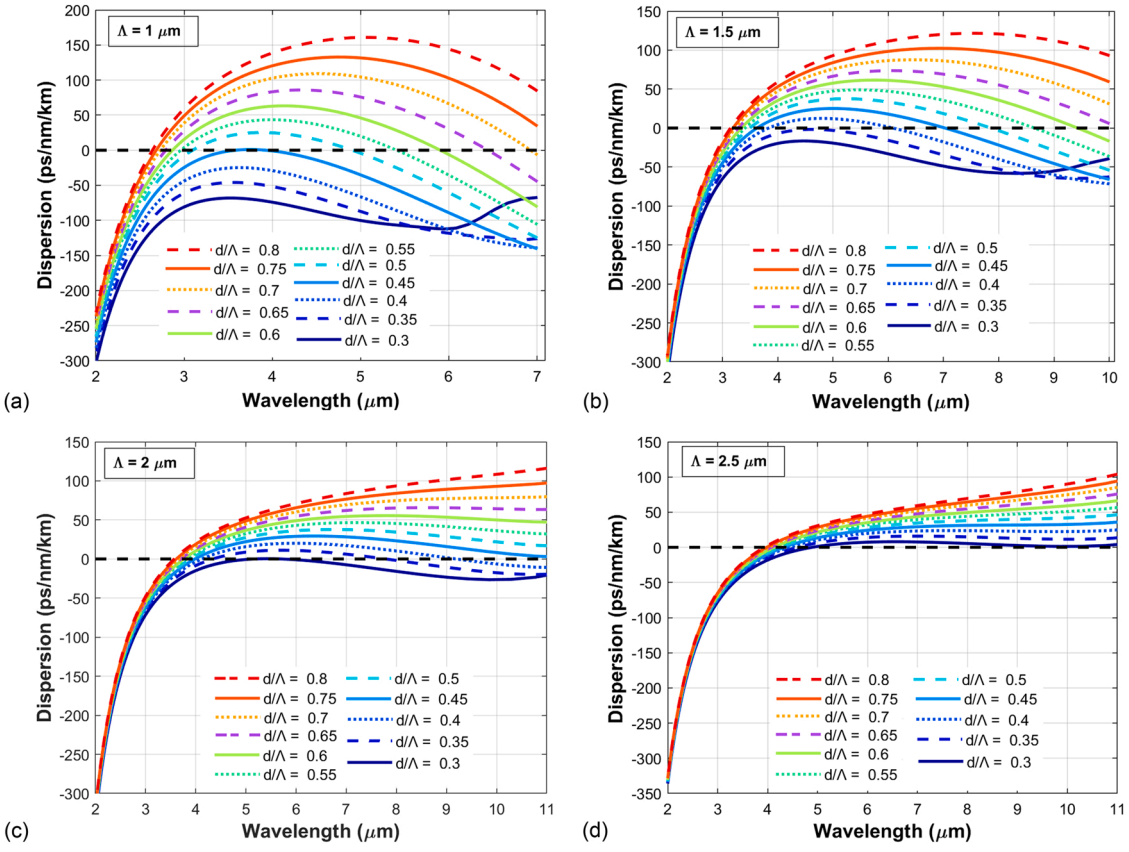


**Fig. 2.** The dispersion of PCF with various values of lattice constant and filling factor.

flat near-zero dispersion shape, and the ZDW compatible with the pump wavelength. Relying on the preliminary simulation, two fibers with structure parameters as shown in Table 2 are selected to analyze the SCG because they have the flat near-zero dispersion in the mid-IR range. They are labeled as #$F_1$ and #$F_2$ fiber. The fibers with $\Lambda = 1$ μm can offer the flat all-normal dispersion, however, they have a smaller core diameter than that of #$F_1$ fiber. The small core results in a high confinement loss at the long-wavelength range, and thus, it reduces the spectral broadening and brightness of SCG in the long-wavelength range. #$F_1$ fiber has a flat all-normal dispersion. The dispersion varies from – 60 to − 1.7 ps/nm/km in the wavelength range of 3–4.6 μm, and it is further flat in the longer wavelength range. At $\lambda = 10$ μm, the dispersion is − 62 ps/nm/km, Fig. 3. Thus, #$F_1$ fiber is used for broad all-normal dispersion SCG. Meanwhile, #$F_2$ fiber has two ZDWs at 4.3 μm ($ZDW_1$) and 7.8 μm ($ZDW_2$). The maximum value of anomalous dispersion is 11.2 ps/nm/km at 5.7 μm, Fig. 3. #$F_2$ fiber is used for broad soliton-induced SCG.

$As_2Se_3$ has high transparency from 2 μm to 14 μm [44], and the high nonlinear refractive index of $As_2Se_3$ allows to the use of the short fiber sample (few centimeters) for broad SCG. Thus, the effects of material loss are neglected. Fig. 4 presents the confinement loss of the proposed fibers. #$F_1$ fiber has low loss in the short wavelengths (below 8 μm), however, the loss dramatically increases in the long-wavelength because this fiber has a small core diameter compared to wavelength in this range. Based on the confinement loss, it is possible to predict that #$F_1$ fiber does not support the guide mode inside the core at the long-wavelengths ($\lambda > 10$ μm). #$F_2$ fiber has a low confinement loss and can be used for broad SCG in a further long wavelength range.

Fig. 5 presents the effective mode areas and nonlinear coefficients of the proposed PCFs. With the small core diameter, #$F_1$ fiber has a smaller effective mode area than that of #$F_2$ fiber with a wavelength below 9.5 μm. However, with $\lambda > 9.5$ μm, the light is no longer confined strongly inside the core. It means that a part of light propagates in the cladding region. Consequently, #$F_1$ fiber has a larger effective mode area than that of #$F_2$ fiber with $\lambda > 9.5$ μm. This also leads to the high confinement loss in this wavelength range as shown in Fig. 4. Effective mode area of #$F_1$ fiber varies from 11.5 to 45 $\mu m^2$ in the wavelength range of 2–10 μm, while that of #$F_2$ fiber varies from 20 to 50 $\mu m^2$ in the wavelength range of 2–11 μm.

The nonlinear coefficient γ is calculated by the equation $\gamma = 2\pi n_2/(\lambda A_{eff})$, where $A_{eff}$ is the effective mode area for the fundamental mode of the fiber. With the high nonlinear refractive index of $As_2Se_3$, the proposed PCFs have large nonlinear coefficients. Since #$F_1$ fiber has smaller effective mode areas in the short-wavelength range ($\lambda < 9.5$ μm), this fiber has higher nonlinear coefficient than that of #$F_2$ fiber. Nonlinear coefficient of the fibers decreases almost linearly with wavelength. In the case of #$F_1$ fiber, the nonlinear coefficient decreases from 2850 to 750 ($W^{-1}km^{-1}$) in the wavelength range of 2–10 μm, while the nonlinear coefficient of #$F_2$ fiber decreases from 1660 to 695 ($W^{-1}km^{-1}$) in the wavelength range of 2–11 μm, Fig. 5(b).

## 3. Supercontinuum generation in proposed fiber

The evolution of the pulses propagating in the investigated fibers is numerically calculated solving GNLSE, using the symmetry split-step Fourier transform method [46]:

**Tablele 2**
The structure parameters of proposed PCFs.

| # | Lattice constant (μm) | Filling factor | Cladding hole diameter (μm) | Core diameter (μm) |
|---|---|---|---|---|
| #$F_1$ | 1.5 | 0.35 | 0.52 | 5.48 |
| #$F_2$ | 2 | 0.35 | 0.7 | 7.3 |

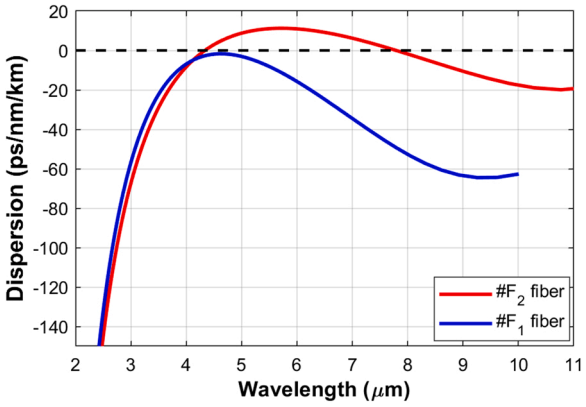


**Fig. 3.** Dispersion characteristics of #$F_1$ and #$F_2$ fiber.

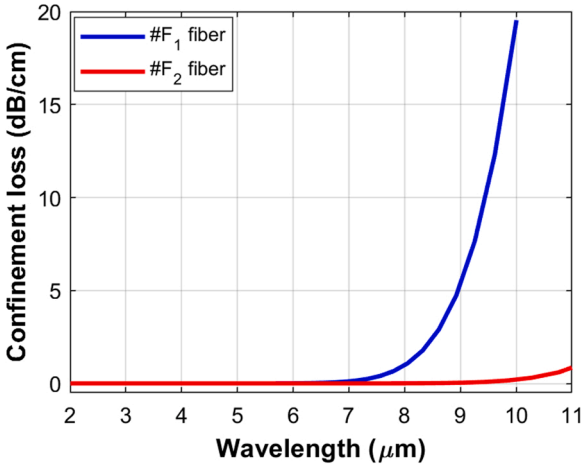


**Fig. 4.** The confinement loss of proposed PCFs.

$$\partial_z \widetilde{A} - i\widetilde{\beta}(\omega)\widetilde{A} - \frac{\widetilde{\alpha}(\omega)}{2}\widetilde{A} = i\gamma\left(1 + \frac{\omega - \omega_0}{\omega_0}\right)\widetilde{A}\mathscr{F}\left[\int_{-\infty}^{\infty} R(T')|A|^2(T - T')dT'\right], \tag{3}$$

where $\widetilde{A}(z,\omega)$ is Fourier transform of the amplitude of a pulse $A(z,T)$, and $R(T)$ is Raman response function.

The left side of Eq. (3) presents the effects of the linear operations, i.e., attenuation and dispersion of the fiber. $\widetilde{\alpha}$ and $\widetilde{\beta}$ are attenuation and dispersion in the frequency domain, respectively, and they are extracted from values shown in Fig. 3 and Fig. 4. In our numerical modeling, the high-order dispersions are calculated through the Taylor series expansion coefficients of the propagation constant at the pumping pulse frequency. The high order of dispersion (from second to eighth order) is shown in Table 3.

The right side of the equation models nonlinear effects, which depend on the nonlinear properties of $As_2Se_3$. The term $\gamma(\omega)$ stands for frequency-dependent nonlinear coefficient as shown in Fig. 5. Nonlinear response function $R(T)$ consist of the electron-bound nonlinearity and molecular nonlinearity in which electron-bound nonlinearity is an instantaneous mechanism since it responds to the effects of the external field in a very short time compared to the pulse duration. *R(T)* is presented as given in Eq. (4) [47].

$$R(T) = (1 - f_R)\delta(T) + f_R h_R(T) \tag{4}$$

where $f_R = 0.148$ [48] is the fractional contribution of delayed Raman response, δ(*T*) is Dirac delta function, *h(T)* represents the retarded

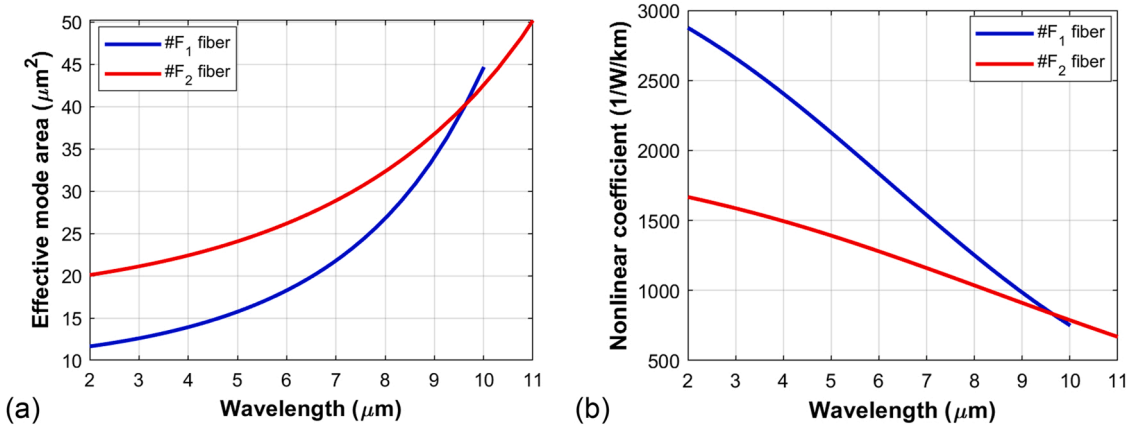


**Fig. 5.** Effective mode area (a) and nonlinear coefficient (b) of the proposed PCFs.

**Table 3**
The coefficient of high order dispersion at pump wavelength (3.5 μm).

| Coefficient | #$F_1$ fiber | #$F_2$ fiber |
|---|---|---|
| $\beta_2$ ($ps^2$/m) | 2.134 ⨩ $10^{-1}$ | 1.885 ⨩ $10^{-1}$ |
| $\beta_3$ ($ps^3$/m) | 9.395 ⨩ $10^{-4}$ | 1.624 ⨩ $10^{-3}$ |
| $\beta_4$ ($ps^4$/m) | 4.757 ⨩ $10^{-6}$ | -3.436 ⨩ $10^{-6}$ |
| $\beta_5$ ($ps^5$/m) | -8.28 ⨩ $10^{-8}$ | 1.286 ⨩ $10^{-8}$ |
| $\beta_6$ ($ps^6$/m) | 1.615 ⨩ $10^{-9}$ | 6.1 ⨩ $10^{-11}$ |
| $\beta_7$ ($ps^7$/m) | -2.71 ⨩ $10^{-11}$ | -3.44 ⨩ $10^{-12}$ |
| $\beta_8$ ($ps^8$/m) | 7.7 ⨩ $10^{-14}$ | 2.54 ⨩ $10^{-13}$ |
| $\beta_9$ ($ps^9$/m) | 5 ⨩ $10^{-15}$ | -7 ⨩ $10^{-15}$ |

response.

The form of $h_R(T)$ in turn takes the approximate analytic form as given in Eq. (5) [47]:

$$h_R(T) = \frac{\tau_1^2 + \tau_2^2}{\tau_1 \tau_2^2} exp\left(\frac{-T}{\tau_2}\right) sin\left(\frac{T}{\tau_1}\right) \Theta(T) \tag{5}$$

where $\Theta(T)$ is Heaviside step function, $\tau_1 = 23.1$ fs, and $\tau_2 = 164.5$ fs [48].

Coherence of SCG is determined by using the first-order coherence according to Eq. (6) [7]:

$$\left| g_{12}^{(1)}(\omega) \right| = \left| \frac{\left\langle \widetilde{A}_i^*(\omega) \widetilde{A}_j(\omega) \right\rangle_{i \neq j}}{\left[ \left\langle \left| \widetilde{A}_i(\omega) \right|^2 \right\rangle \left\langle \left| \widetilde{A}_j(\omega) \right|^2 \right\rangle \right]^{1/2}} \right| \tag{6}$$

where $\widetilde{A}_i(\omega) = \widetilde{A}_i(z, \omega)$, subscripts $(i,j)\epsilon$, [1,20] and the angle brackets denote ensemble average over independently generated SC spectra with input noises.

The average of the coherence across entire the SC spectrum is calculated as given in Eq. (7) [49]:

$$\left\langle \left| g_{12}^{(1)} \right| \right\rangle = \frac{\int_0^\infty \left| g_{12}^{(1)}(\omega) \right| \left\langle \left| \widetilde{A}_i(\omega) \right|^2 \right\rangle d\omega}{\int_0^\infty \left\langle \left| \widetilde{A}_i(\omega) \right|^2 \right\rangle d\omega} \tag{7}$$

The laser pulses used in the simulations are modeled by a Gaussian pulse centered at the pumping wavelength and are expressed as given in Eq. (8):

$$A(T) = \sqrt{P_0} \exp\left(\frac{-T^2}{2t_0^2}\right) \tag{8}$$

where $P_0$ is peak power, $t_0$ is pulse duration.

In the simulation, we use the pump wavelengths at 3.5 μm and 5.5 μm. The pump wavelength at 3.5 μm is near $ZDW_1$ while the pump wavelength at 5.5 μm located in the further flat dispersion of #$F_1$ fiber. The difference frequency generation (DFG) laser systems pumped by a Ti:Sapphire mode-locked laser (Verdi– Coherent Mira 900 – Legend – Topas) can generate femtosecond pulses with the tunable wavelength from 2.5 to 12 μm, and the pulse duration is near 200 fs [41]. Therefore, in simulation for SCG in proposed PCFs, the pulse duration of 200fs is chosen.

The proposed fibers are multi-mode guidance at pump wavelength (3.5 μm). In particular, #$F_1$ fiber has two modes ($LP_{01}$ and $LP_{11}$) and #$F_2$ fiber has three modes ($LP_{01}$, $LP_{11}$ and $LP_{31}$). However, the high-order modes do not significantly influence spectral broadening along fiber with short duration of input laser pulses (< 10 ps) because the walk-off between the fundamental mode and high-order modes is long enough to prevent the energy transfer from the fundamental mode to high-order modes [50]. Therefore, only fundamental mode is considered for SCG analysis according to Eq. (3).

The characteristic lengths of pulse broadening dynamics as shown in a set of the following Eq. (9) are used to analyze the nonlinear properties of the investigated fibers [7]:

$$L_D = \frac{t_0^2}{|\beta_2|}, \quad L_{NL} = \frac{1}{\gamma P_0}, \quad N = \sqrt{\frac{L_D}{L_{NL}}}, L_{WB} \approx 1.1 \frac{L_D}{N} \tag{9}$$

where $L_D$, $L_{NL}$ are dispersive, nonlinear characteristic length scales, respectively. $N$ is soliton number, $P_0$ and $t_0$ are peak power and pulse duration of an input pulse. The parameter $\beta_2$ represents the group velocity dispersion at the central wavelength of the input laser pulse. $L_{WB}$ is an optical wave-breaking length.

The spectral broadening in #$F_1$ fiber is induced by self-phase modulation (SPM) followed by optical wave breaking (OWB) as a typical mechanism for all-normal dispersion spectral broadening. Fig. 6(a,b) present the evolution of SC spectra at 2.5 cm of propagation as a function of input pulse energy, which was set up in the range 0.01–1.5 nJ, corresponding to the peak power 0.05–7.5 kW. In the case of low input pulse energy, the SC spectrum is induced by SPM that is accompanied by an oscillatory structure covering the entire spectrum. The SPM-induced spectrum consists of many peaks and the outermost peak has the most intense, Fig. 6(b). With the further increase of the input pulse energy (higher than 0.1 nJ), the center of the spectrum is induced by SPM, and then OBW contributes to the spectral broadening at the wings, Fig. 6(b). In the case of input pulse energy of 1 nJ, the SC spectrum spans in the wavelength range of 2–5.5 μm within 5 dB dynamics.

The pulse evolution in the #$F_1$ with input pulse energy of 1 nJ is presented in Fig. 6(c). The spectral broadening is induced by SPM at the beginning of the propagation. The spectrum is asymmetry toward the short wavelength range via the effects of nonlinear dispersion, e.g., self-steepening. The SPM-induced spectrum experiences effects of the

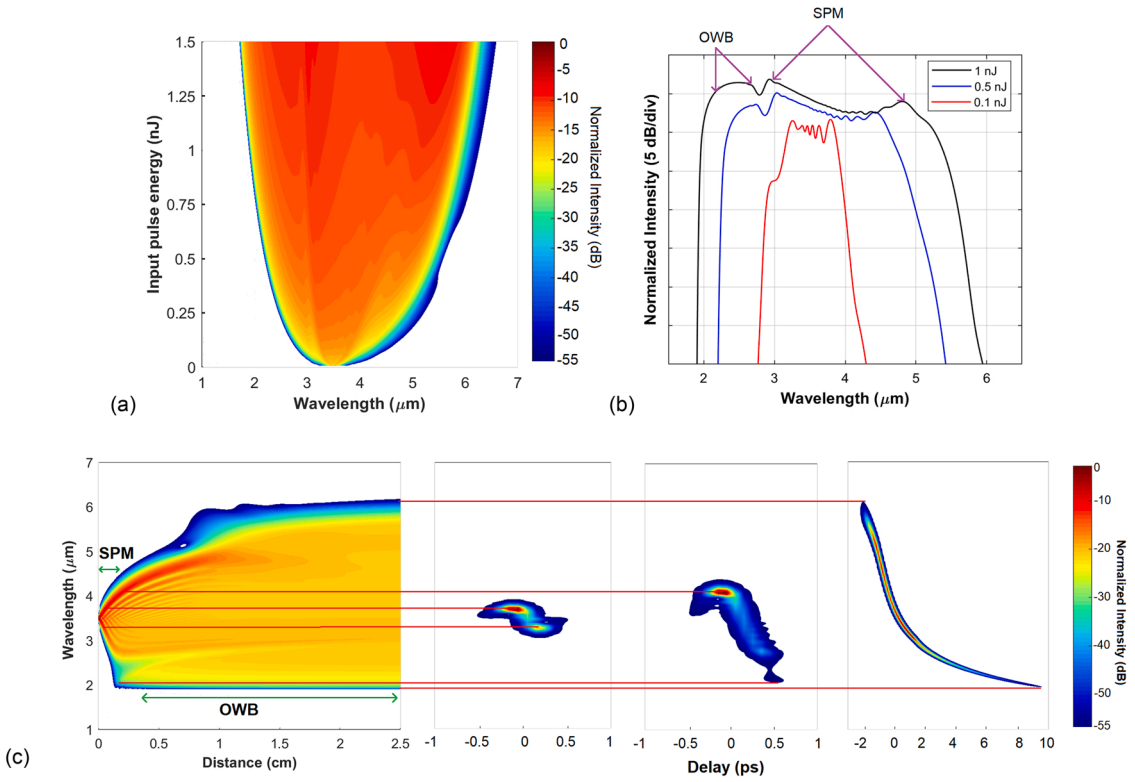


**Fig. 6.** The evolution of spectral bandwidth of SCG in #$F_1$ fiber (a), SC spectrum at 2.5 cm of propagation (b), and evolution of pulse in #$F_1$ fiber with input peak power of 5 kW (left panel) and temporal profile at various positions of the propagation (right panel) (c).

dispersion in further propagation, and the short-wavelength at the trailing edge propagates slower than the pulse tail at the center of the pulse. The temporal overlap between the pulse tail and trailing edge leads to the onset of OWB, and the new wavelengths can be created via four-wave mixing (FWM). The FWM-induced wavelength can be estimated as given in Eq. (10) [47]. For example, the SPM-induced wavelength at 2.9 μm acts as the pump, and the pulse tail at 3.5 μm acts as the seed. Consequently, FWM creates the wavelength component at 2.4 μm.

$$\omega_{FWM} = 2\omega_{pump} - \omega_{seed} \leftrightarrow \frac{1}{\lambda_{FWM}} = \frac{2}{\lambda_{pump}} - \frac{1}{\lambda_{seed}} \tag{10}$$

The new wavelength induced by FWM contributes to the OWB, thus OWB occurs firstly at the trailing edge of the pulse. At pump wavelength (3.5 μm), #$F_1$ fiber has $\beta_2 = -0.2$ ($ps^2$/m). The characteristic lengths of #$F_1$ fiber is $L_D = 18$ cm, $L_{NL} = 0.014$ cm, and $L_{WB} = 0.5$ cm. At the leading edge of the pulse, OWB also occurs around 1 cm of propagation and generates the new wavelength band around 5.5 μm. During further propagation, the spectral broadening at the trailing edge of the pulse is restricted by the high steepness of the dispersion characteristics. At the leading edge, the large effective mode area results in a low nonlinear coefficient and limits the spectral broadening. Fig. 6(c) (right panel) shows the temporal profile of the spectrum at the various lengths of propagation. In the time domain, this trace is trenched out during the propagation due to the effects of dispersion. However, no new wavelength components are created herein.

The coherence of supercontinuum generation depends on the effects of the input noise, such as vacuum noise, pulse-to-pulse noise, polarization noise. In the numerical model to estimate the coherence of SCG, vacuum noise relates to nonlinear amplification of quantum fluctuations, and it is calculated by the addition of one photon with random phase per each simulation bin. The pulse-to-pulse noise is the amplitude fluctuation of each input pulse. The amplitude fluctuation also leads to the fluctuation of the pulse duration, as shown in Eq. (11) [42]:

$$\delta t_0 = -0.8 \times (\delta A_{AN} - 1) \tag{11}$$

where $\delta A_{AN}$ is a single random value. The means of $\delta A_{AN}$ is equal to 1 and its root-mean-square (rms) is given by the manufacturer of the lasers. In fact, rms of the femtosecond laser take the value from 0.5% to 1%. $\delta t_0$ is the pulse duration fluctuation. The numerical model of input pulse with vacuum noise and pulse-to-pulse noise follows the formalist proposed in [42]. Here, we do not consider the effects of polarization noise. However, with the use of a short fiber sample (2.5 cm) and short pulse duration, the polarization noise may not influence the coherent characteristics [51].

The coherent characteristics of the SCG are shown in Fig. (7). If only vacuum noise is taken into account, this noise is suppressed in a normal dispersion regime, and thus the SCG has high coherence across the entire spectrum. However, the pulse-to-pulse noise is not mitigated herein, and it causes significant degradation of the coherence. As shown in Fig. 7(a), the center of the spectrum induced by SPM has higher coherence than that of the wings. In the other words, the laser noise dramatically reduces the coherence of wavelength components that are generated by OWB and FWM. In addition, the leading edge experiences less degradation of coherence than that of the trailing edge because the large confinement loss and large effective mode area are restricted to the new wavelength created by OWB.

Fig. 7(b) presents the average of coherences with the various values of $\delta A_{AN}$ and pulse duration for input peak power of 5.5 kW and fiber sample length of 2.5 cm. The effects of pulse-to-pulse noise on the coherence depend on the laser pulse duration. In particular, the SCG pumped by the short laser pulse (<100 fs) has the average coherence $\left\langle \left| g_{12}^{(1)} \right| \right\rangle > 0.9$ with any value of $\delta A_{AN}$. However, the use of a long-pulse laser causes a decrease of coherence. With a pulse duration of 500fs, and $\delta A_{AN} = 1\%$, the SCG exhibits low coherence with $\left\langle \left| g_{12}^{(1)} \right| \right\rangle \approx 0.2$.

The all-normal dispersion SCG is generated by SPM, and OWB

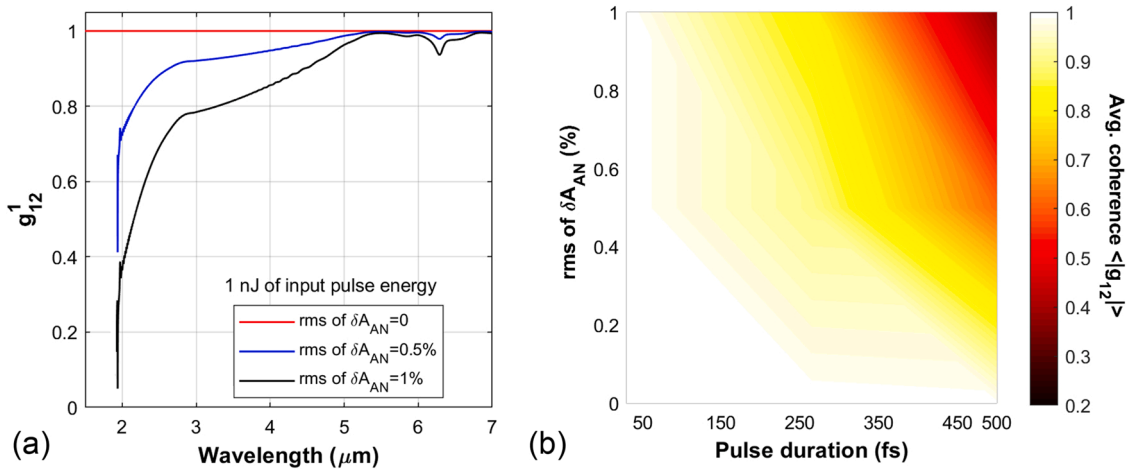


**Fig. 7.** The first-order coherence of the SCG in #$F_1$ fiber with input pulse energy of 1 nJ (peak power of 5 kW) and different values of root-mean-square of the laser (a). The average of coherence with the various values of pulse duration, and $\delta A_{AN}$ (b). The coherent characteristics are calculated with 20 SCG simulations with random values of noise seeds.

induced by FWM. During further propagation, the FWM and OWB only transfer the light energy from the center of the pulse to the edges and make a further smooth spectrum. Moreover, the transferred energy by FWM occurs only in the instant of temporal overlap of pump and seed. Therefore, the spectral bandwidth solely depends on the amount of SPM-induced spectral broadening before OWB occurs. For instance, #$F_1$ fiber has the flat dispersion in the mid-IR range, thus, the use of pump wavelength at 5.5 μm enables the generation of the SPM-induced spectrum with a broader spectral bandwidth, from 4 to 7 μm. The broad SPM-induced spectrum, in turn, offers the broad spectrum generated by OWB, from 1.9 to 3.8 μm, Fig. 8. Consequently, using pump wavelength at 5.5 μm, #$F_1$ fiber offers the flat-top broadband SCG with low input peak power. As shown in Fig. 8, with input peak power of 5 kW, #$F_1$ fiber can offer 2-octave spanning SCG with a spectral bandwidth of 1.9–7.6 μm in 10 dB dynamics.

#$F_2$ fiber has dispersion characteristics with both normal and anomalous regimes in the investigated wavelength range, and soliton dynamics are the main contributions to the spectral broadening. Thus, SCG in #$F_2$ fiber has a much broader spectral bandwidth than that of all-normal dispersion SCG. Fig. 9(a) and (b) present the evolution of SC spectrum at 5 cm of propagation with input pulse energy from 0.001 nJ to 2 nJ, corresponding to the input peak power from 0.005 kW to 10 kW. In the case of low input pulse energy (below 0.8 nJ), the spectral bandwidth exponentially increases with the energy of the pulses. However, the high steep dispersion in the short wavelengths and large mode area in the long-wavelength lead to the limitation of spectral broadening, thus, the spectral bandwidth is almost constant with further increase of input pulse energy, Fig. 9(a). With an input pulse energy of 1.5 nJ (peak power of 7.5 kW), the SCG has multi octave-spanning, from 2 μm to 10 μm within 20 dB dynamics, Fig. 9(b).

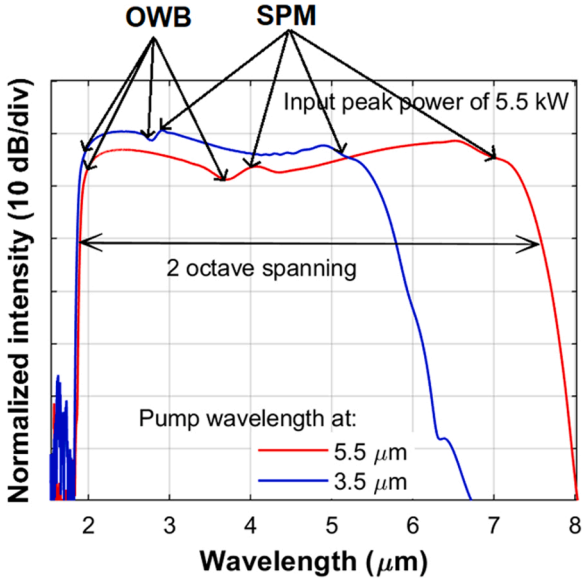


**Fig. 8.** The output spectrum with pump wavelength at 3.5 μm and 5.5 μm. The input peak power of 5 kW.

The pulse evolution in #$F_2$ fiber with an input pulse energy of 1.5 nJ is presented in Fig. 9(c). At the beginning of the propagation, the spectral broadening is induced by SPM with the temporal profile in the S-shape. When the distance of propagation is 0.3 cm, the trailing of the SPM-induced spectrum interferes with the pulse tail. As a result, the new wavelength band around 2 μm is generated by FWM, and it is attributed to OWB. #$F_2$ fiber has $\beta_2 = 0.187$ ($ps^2$/m) at pump wavelength (3.5 μm). According to Eq. (9), the OWB length of this fiber is 0. 6 cm – well matching with Fig. 9(c). At the leading edge of the pulse, when the SPM-induced spectrum reaches the $ZDW_1$ at 4.3 μm, a part of the spectrum propagates in the anomalous dispersion regimes and it behaves like soliton. Because the value of $\beta_2$ is low at near ZDW, the soliton herein has a high soliton-number. Due to the effects of high-order dispersion, the soliton fission occurs to eject the fundamental solitons. As shown in Fig. 9(c), the soliton fission occurs around 2.5 cm of propagation. #$F_2$ fiber has $ZDW_2$ at 7.8 μm, and dispersion shape near $ZDW_2$ has a negative slope. Thus, during further propagation, the combination between the negative slope of dispersion and anomalous dispersion regime leads to the red-shifted dispersive wave (DW). As a result, new wavelengths around 10 μm are created. At the trailing edge, the blue-shifted DW generates wavelengths around 2.5 μm. Thus, the dynamic at the trailing edge is complicated including the SPM and OWB accompanied by the blue-shifted DW.

Coherence of SCG in #$F_2$ fiber is shown in Fig. 10. Because #$F_2$ fiber has flat near-zero dispersion, soliton fission and dispersive wave can completely occur before the modulation instability (MI) has the significant effects to amplify the vacuum noise. Therefore, if only vacuum noise is considered, the soliton-induced SCG #$F_2$ fiber has not experienced significant decoherence. However, pulse-to-pulse noise dramatically reduces the coherence. The amount of coherence degradation also depends on the mechanism for spectral broadening as in the case of all-normal dispersion SCG. In the short wavelength range (below $ZDW_1$), the spectrum is induced by OWB and DW. It is worth noting that DW

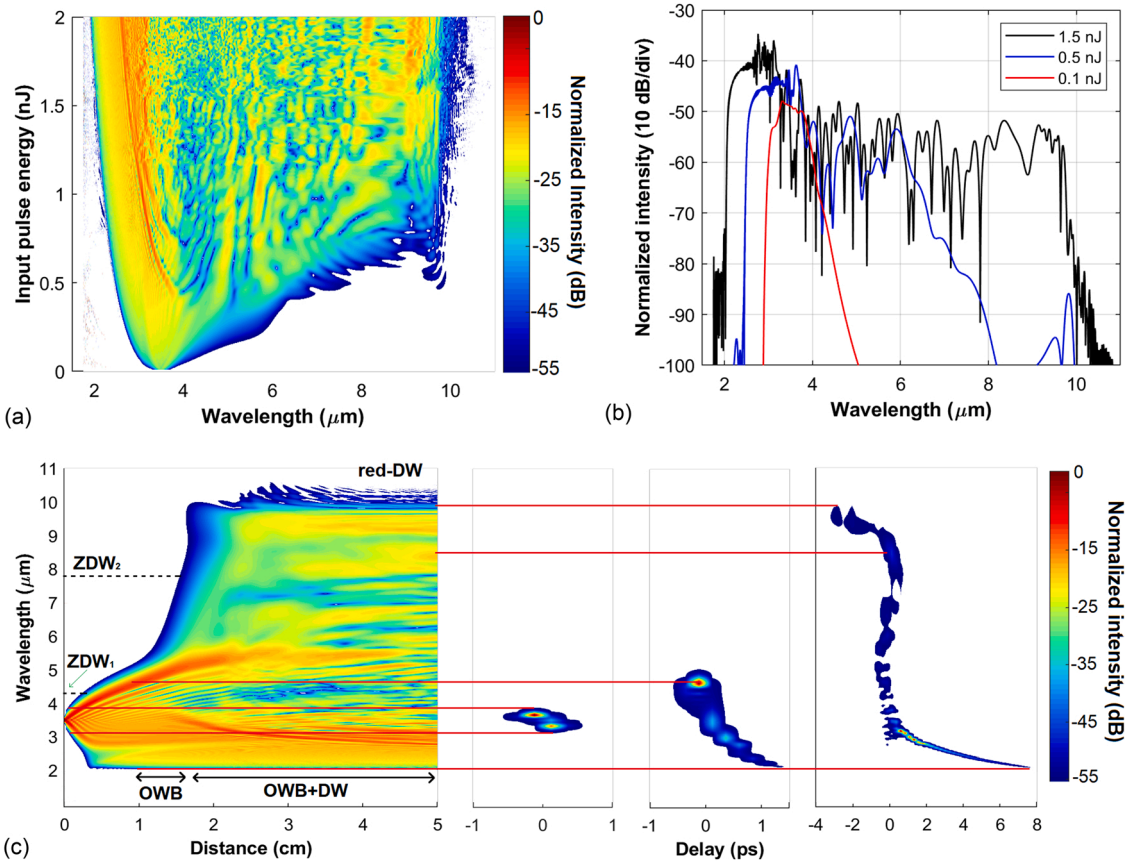


**Fig. 9.** The evolution of spectral bandwidth of SCG in #$F_2$ fiber (a), SC spectrum at 5 cm of propagation (b), and evolution of pulse in #$F_2$ fiber with input peak power of 7.5 kW (left panel) and temporal profile at various positions of the propagation (right panel) (c).

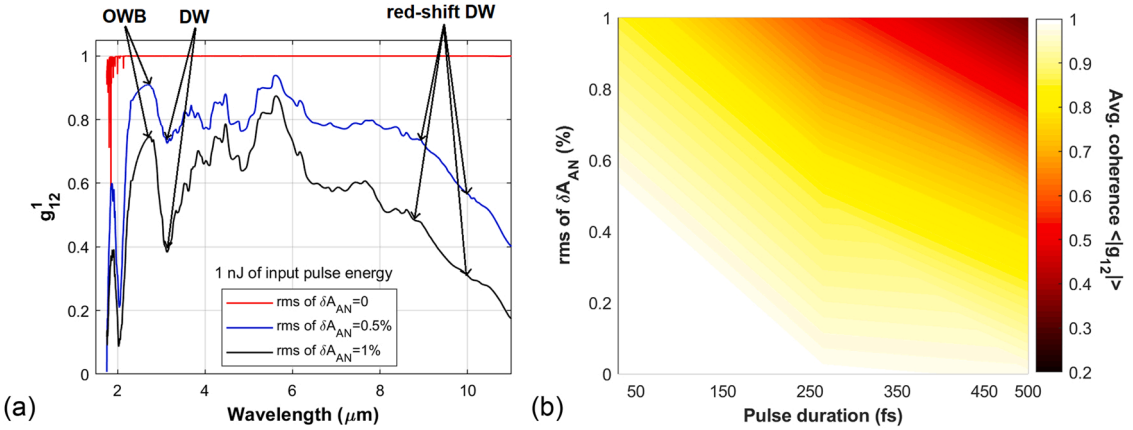


**Fig. 10.** The first-order coherence of the SCG in #$F_1$ fiber with input pulse energy of 1.5 nJ (peak power of 7.5 kW) and different values of root-mean-square of the laser (a). The average of coherence with the various values of pulse duration, and $\delta A_{AN}$ (b). The coherent characteristics are calculated with 20 SCG simulations with random values of noise seeds.

strongly depends on the frequency and peak power of the fundamental solitons after soliton fission [7]. For instance, the relation of DW with frequency $\omega_{DW}$ and a soliton with frequency $\omega_S$ and peak power $P_S$ is given as in Eq. (12) [7]:

$$\beta(\omega_S) - \frac{\omega_S}{\nu_{g,S}} + (1 - f_R)\gamma P_S = \beta(\omega_{DW}) - \frac{\omega_{DW}}{\nu_{g,S}} \tag{12}$$

The pulse-to-pulse noise leads to fluctuation of the fundamental solitons, this leads to the intensity and phase fluctuation of DW. Therefore, the spectrum induced by DW, in both trailing and leading edge, has lower coherence compared to another part of the spectrum, Fig. 10 (a).

Fig. 10(b) shows the value of average spectral coherence of SC spectrum with input peak power of 7.5 kW as a function of pulse duration and $\delta A_{AN}$. The femtosecond laser with low pulse-to-pulse noise ($\delta A_{AN} < 0.2\%$) generate the high coherent SCG with $\left\langle \left| g_{12}^{(1)} \right| \right\rangle > 0.9$ with long pulse duration laser. In contrast, the high pulse-to-pulse noise causes a significant decrease of coherence, such as $\delta A_{AN} = 1\%$ leads to $\left\langle \left| g_{12}^{(1)} \right| \right\rangle \approx 0.6$ with pulse duration of 200 fs, and $\left\langle \left| g_{12}^{(1)} \right| \right\rangle \approx 0.2$ with

pulse duration of 500 fs.

## 4. Conclusion

We reported the numerical simulation for SCG in $As_2Se_3$ PCFs with the femtosecond lasers as the pump sources. The proposed PCFs were selected from the preliminary fiber design with the modification of structure parameters. Two proposed fibers have flat dispersion in the investigated wavelength range of 2–11 μm, and they enable board SCG with low input peak powers. These fibers also have larger core diameters than that of the fibers in previous works [30–33,35–40]. Thus, they have the potential for the high coupling efficiency of the light into the proposed fibers if the free-space coupling is used, and the high coupling efficiency between these fibers and standard fibers if a compact all-fiber SCG system is considered.

$\#F_1$ fiber with a lattice constant of 1.5 μm, core diameter of 5.48 μm has flat all-normal dispersion in the investigated wavelength range. With the use of the femtosecond laser with pump wavelength at 3.5 μm, pulse duration of 200 fs, and input peak power of 5 kW, $\#F_1$ fiber generated the SCG with a spectral bandwidth of 1.85–5.5 μm within 8 dB dynamics. The SCG is induced by SPM at the center of the spectrum and OWB at the spectrum wings. With the flat dispersion of $\#F_1$ fiber, the use of 5.5 μm pump wavelength enabled the flat-top SCG with two-octave spanning – from 1.9 to 7.6 μm within 10 dB.

$\#F_2$ fiber, with lattice constant of 2 μm and core diameter of 7.3 μm, has two zero-dispersion wavelengths with $ZDW_1$ at 4.3 μm and $ZDW_2$ at 7.8 μm. The SCG in $\#F_2$ fiber is mainly induced by soliton dynamics in which the solitons are contracted in the anomalous dispersion regime, and the spectrum in the normal dispersion is induced by DW. The OWB also contributes to spectral broadening at the trailing edge of the spectrum. With the use of input peak power of 7.5 kW, pulse duration of 200 fs, and pump wavelength at 3.5 μm, $\#F_2$ fiber offers the broad SCG with a spectral bandwidth of 2–10 μm within 20 dB.

SCG in both $\#F_1$ and $\#F_2$ fiber has a high coherence when only vacuum noise is considered. However, pulse-to-pulse relative intensity noise leads to the significant degradation of coherence if a long pulse laser is used. The effects of this noise also depend on the physical mechanisms for spectral broadening, pulse duration. For all-normal dispersion SCG, the spectrum induced by SPM (center of the spectrum) exhibits higher coherence than that of wings of the spectrum induced by OWB. For SCG in $\#F_2$ fiber, the OWB at the trailing edge and soliton in the center of the spectrum has higher coherences than the blueshift and redshift DW.

The proposed fibers offer the multi-octave spanning SCG with much lower input peak power when compared to previous works [33,35–39,41]. The low input peak power and large core give the proposed fibers a high potential for a compact all-fiber SCG system. The SCG in proposed fibers has a potential for high coherence. Thus, they are possible to use for applications in the mid-IR range, such as multimodal biophotonic imaging, multibeam pump-probe techniques. Moreover, the flat-top 2-octave spanning SCG in $\#F_1$ fiber is found to be suitable for nonlinear pulse compression, $f-2f$ or $2f-3f$ interferometry.

## Declaration of Competing Interest

The authors declare that they have no known competing financial interests or personal relationships that could have appeared to influence the work reported in this paper.

## Acknowledgments

This research is funded by Vietnam National Foundation for Science and Technology Development (NAFOSTED) under grant number 103.03-2020.03; Vietnam's Ministry of Education and Training (B2021-DHH-08).

*Declaration of Competing Interest*

The authors report no declarations of interest.

## References

[1] G. Humbert, W.J. Wadsworth, S.G. Leon-Saval, J.C. Knight, T.A. Birks, P. St. J. Russell, M.J. Lederer, D. Kopf, K. Wiesauer, E.I. Breuer, D. Stifter, Supercontinuum generation system for optical coherence tomography based on tapered photonic crystal fibre, Opt. Express 14 (4) (2006) 1596–1603, https://doi.org/10.1364/OE.14.001596.

[2] N.M. Israelsen, C.R. Petersen, A. Barh, D. Jain, M. Jensen, G. Hannesschläger, P. Tidemand-Lichtenberg, C. Pedersen, A. Podoleanu, O. Bang, Real-time high-resolution mid-infrared optical coherence tomography, Light Sci. Appl. 8 (1) (2019) 11, https://doi.org/10.1038/s41377-019-0122-5.

[3] J.T. Woodward, A.W. Smith, C.A. Jenkins, C. Lin, S.W. Brown, K.R. Lykke, Supercontinuum sources for metrology, Metrologia 46 (4) (2009) S277–S282, https://doi.org/10.1088/0026-1394/46/4/S27.

[4] D.R. Carlson, D.D. Hickstein, A. Lind, J.B. Olson, R.W. Fox, R.C. Brown, A. D. Ludlow, Q. Li, D. Westly, H. Leopardi, T.M. Fortier, K. Srinivasan, S.A. Diddams, S.B. Papp, Photonic-chip supercontinuum with tailored spectra for counting optical frequencies, Phys. Rev. Appl. 8 (2017), 014027, https://doi.org/10.1103/PhysRevApplied.8.014027.

[5] C. Poudel, C.F. Kaminski, Supercontinuum radiation in fluorescence microscopy and biomedical imaging applications, J. Opt. Soc. Am. B 36 (2) (2019) A139–A153, https://doi.org/10.1364/JOSAB.36.00A139.

[6] C.R. Petersen, P.M. Moselund, L. Huota, L. Hooper, O. Bang, Towards a table-top synchrotron based on supercontinuum generation, Infrared Phys. Technol. 91 (2018) 182–186, https://doi.org/10.1016/j.infrared.2018.04.008.

[7] J.M. Dudley, G. Genty, S. Coen, Supercontinuum generation in photonic crystal fiber, Rev. Mod. Phys. 78 (4) (2006) 1135–1184, https://doi.org/10.1103/RevModPhys.78.1135.

[8] M. Chemnitz, M. Gebhardt, C. Gaida, F. Stutzki, J. Kobelke, J. Limpert, A. Tünnermann, M.A. Schmidt, Hybrid soliton dynamics in liquid-core fibres, Nat. Commun. 8 (2017) 42, https://doi.org/10.6084/m9.figshare.4816462.

[9] M. Chemnitz, R. Scheibinger, C. Gaida, M. Gebhardt, F. Stutzki, S. Pumpe, J. Kobelke, A. Tünnermann, J. Limpert, M.A. Schmidt, Thermodynamic control of soliton dynamics in liquid-core fibers, Optica 5 (6) (2018) 695–703, https://doi.org/10.1364/OPTICA.5.000695.

[10] V.T. Hoang, R. Kasztelanic, G. St˛epniewski, K.D. Xuan, V.C. Long, M. Trippenbach, M. Klimczak, R. Buczyński, J. Pniewski, Femtosecond supercontinuum generation around 1560 nm in hollow-core photonic crystal fibers filled with carbon tetrachloride, Appl. Opt. 59 (12) (2020) 3720–3725, https://doi.org/10.1364/AO.385003.

[11] L.C. Van, V.T. Hoang, V.C. Long, K. Borzycki, K.D. Xuan, V.T. Quoc, M. Trippenbach, R. Buczyński, J. Pniewski, Supercontinuum generation in photonic crystal fibers infiltrated with nitrobenzene, Laser Phys. 30 (3) (2020), 035105, https://doi.org/10.1088/1555-6611/ab6f09.

[12] H.V. Le, V.T. Hoang, H.T. Nguyen, V.C. Long, R. Buczynski, R. Kasztelanic, Supercontinuum generation in photonic crystal fibers infiltrated with tetrachloroethylene, Opt. Quant. Electron. 53 (2021) 187, https://doi.org/10.1007/s11082-021-02820-3.

[13] M. Cassataro, D. Novoa, M.C. Günendi, N.N. Edavalath, M.H. Frosz, J.C. Travers, P. S.J. Russell, Generation of broadband mid-IR and UV light in gas-filled single-ring hollow-core PCF, Opt. Express 25 (7) (2017) 7637–7644, https://doi.org/10.1364/OE.25.007637.

[14] A.I. Adamu, M.S. Habib, C.R. Petersen, J.E.A. Lopez, B. Zhou, A. Schülzgen, M. Bache, R. Amezcua-Correa, O. Bang, C. Markos, Deep-UV to mid-IR supercontinuum generation driven by mid-IR ultrashort pulses in a gas-filled hollow-core fiber, Sci. Rep. 9 (1) (2019) 4446–4449, https://doi.org/10.1038/s41598-019-39302-2.

[15] V.T. Hoang, R. Kasztelanic, A. Filipkowski, G. Stępniewski, D. Pysz, M. Klimczak, S. Ertman, V.C. Long, T.R. Woliński, M. Trippenbach, K.D. Xuan, M. Śmietana, R. Buczyński, Supercontinuum generation in an all-normal dispersion large core photonic crystal fiber infiltrated with carbon tetrachloride, Opt. Mater. Express 9 (5) (2019) 2264–2278, https://doi.org/10.1364/OME.9.002264.

[16] M. Klimczak, D. Michalik, G. Stępniewski, T. Karpate, J. Cimek, X. Forestier, R. Kasztelanic, D. Pysz, R. Stępień, R. Buczyński, Coherent supercontinuum generation in tellurite glass regular lattice photonic crystal fibers, J. Opt. Soc. Am. B 36 (2) (2019) A112–A124, https://doi.org/10.1364/JOSAB.36.00A112.

[17] G. Tao, H. Ebendorff-Heidepriem, A.M. Stolyarov, S. Danto, J.V. Badding, Y. Fink, J. Ballato, A.F. Abouraddy, Infrared fibers, Adv. Opt. Photonics 7 (2) (2015) 379–458, https://doi.org/10.1364/AOP.7.000379.

[18] C.R. Petersen, U. Møller, I. Kubat, B. Zhou, S. Dupont, J. Ramsay, T. Benson, S. Sujecki, N. Abdel-Moneim, Z. Tang, D. Furniss, A. Seddon, O. Bang, Mid-infrared supercontinuum covering the 1.4–13.3 μm molecular fingerprint region using ultra-high NA chalcogenide step-index fibre, Nat. Photonics 8 (11) (2014) 830–834, https://doi.org/10.1038/nphoton.2014.213.

[19] S. Dai, Y. Wang, X. Peng, P. Zhang, X. Wang, Y. Xu, A review of mid-infrared supercontinuum generation in chalcogenide glass fibers, Appl. Sci. 8 (5) (2018) 707, https://doi.org/10.3390/app8050707.

[20] A. Lemière, F. Désévédavy, P. Mathey, P. Froidevaux, G. Gadret, J.-C. Jules, C. Aquilina, B. Kibler, P. Béjot, F. Billard, O. Faucher, F. Smektala, Mid-infrared supercontinuum generation from 2 to 14um in arsenic- and antimony-free

chalcogenide glass fibers, J. Opt. Soc. Am. B 36 (2) (2019) A183–A192, https://doi.org/10.1364/JOSAB.36.00A183.
[21] M.K. Dasa, G. Nteroli, P. Bowen, G. Messa, Y. Feng, C.R. Petersen, S. Koutsikou, M. Bondu, P.M. Moselund, A. Podoleanu, A. Bradu, C. Markos, O. Bang, All-fibre supercontinuum laser for in vivo multispectral photoacoustic microscopy of lipids in the extended near-infrared region, Photoacoustics 18 (2020), 100163, https://doi.org/10.1016/j.pacs.2020.100163.
[22] I. Zorin, J. Kilgus, K. Duswald, B. Lendl, B. Heise, M. Brandstetter, Sensitivity-enhanced Fourier transform mid-infrared spectroscopy using a supercontinuum laser source, Appl. Spectrosc. 74 (4) (2020) 485–493, https://doi.org/10.1177/0003702819893364.
[23] C.R. Petersen, N. Prtljaga, M. Farries, J. Ward, B. Napier, G.R. Lloyd, J. Nallala, N. Stone, O. Bang, Mid-infrared multispectral tissue imaging using a chalcogenide fiber supercontinuum source, Opt. Lett. 43 (5) (2018) 999–1002, https://doi.org/10.1364/OL.43.000999.
[24] A.B. Seddon, A prospective for new mid-infrared medical endoscopy using chalcogenide glasses, Int. J. Appl. Glass Sci. 2 (3) (2011) 177–191, https://doi.org/10.1111/j.2041-1294.2011.00059.x.
[25] Z. Zhao, B. Wu, X. Wang, Z. Pan, Z. Liu, P. Zhang, X. Shen, Q. Nie, S. Dai, R. Wang, Mid-infrared supercontinuum covering 2.0-16 μm in a low-loss telluride single-mode fiber, Laser Photonics Rev. 11 (2) (2017), 1700005, https://doi.org/10.1002/lpor.201700005.
[26] N. Zhang, X. Peng, Y. Wang, S. Dai, Y. Yuan, J. Su, G. Li, P. Zhang, P. Yang, X. Wang, Ultrabroadband and coherent mid-infrared supercontinuum generation in Te-based chalcogenide tapered fiber with all-normal dispersion, Opt. Express 27 (7) (2019) 10311–10319, https://doi.org/10.1364/OE.27.010311.
[27] T.S. Saini, T.H. Tuan, T. Suzuki, Y. Ohishi, Coherent mid-IR supercontinuum generation using tapered chalcogenide step-index optical fiber: experiment and modelling, Sci. Rep. 10 (1) (2020) 2236, https://doi.org/10.1038/s41598-020-59288-6.
[28] H.P.T. Nguyen, K. Nagasaka, T.H. Tuan, T.S. Saini, X. Luo, T. Suzuki, Y. Ohishi, Highly coherent supercontinuum in the mid-infrared region with cascaded tellurite and chalcogenide fibers, Appl. Opt. 57 (21) (2018) 6153–6163, https://doi.org/10.1364/AO.57.006153.
[29] S. Venck, F. St-Hilaire, L. Brilland, A.N. Ghosh, R. Chahal, C. Caillaud, M. Meneghetti, J. Troles, F. Joulain, S. Cozic, S. Poulain, G. Huss, M. Rochette, J. M. Dudley, T. Sylvestre, 2–10 μm Mid-infrared fiber-based supercontinuum lasersource: experiment and simulation, Laser Photonics Rev. 14 (6) (2020), 2000011, https://doi.org/10.1002/lpor.202000011.
[30] P. Yan, R. Dong, G. Zhang, H. Li, S. Ruan, H. Wei, J. Luo, Numerical simulation on the coherent time-critical 2–5 mm supercontinuum generation in an As2S3micro-structured optical fiber with all-normal flat-top dispersion profile, Opt. Commun. 293 (2013) 133–138, https://doi.org/10.1016/j.optcom.2012.11.093.
[31] A. Baili, R. Cherif, M. Zghal, Two octaves spanning supercontinuum in highly nonlinear As2Se3 nanophotonic crystal fiber for midinfrared applications, J. Nanophotonics 9 (2015), 093059, https://doi.org/10.1117/1.JNP.9.093059.
[32] S. Vyas, T. Tanabe, M. Tiwari, G. Singh, Chalcogenide photonic crystal fiber for ultraflat mid-infrared supercontinuum generation, Chin. Opt. Lett. 14 (12) (2016) 123201–123205, https://doi.org/10.3788/COL201614.123201.
[33] A. Ben Salem, M. Diouf, R. Cherif, A. Wague, M. Zghal, Ultraflat-top mid-infrared coherent broadband supercontinuum using all normal As2S5-borosilicate hybrid photonic crystal fiber, Opt. Eng. 55 (6) (2016), 066109, https://doi.org/10.1117/1.OE.55.6.066109.
[34] M. Valliammai, S. Sivabalan, Wide-band supercontinuum generation in mid-IR using polarization maintaining chalcogenide photonic quasi-crystal fiber, Appl. Opt. 56 (16) (2017) 4797–4806, https://doi.org/10.1364/AO.56.004797.
[35] M. Kalantari, A. Karimkhani, H. Saghaei, Ultra-Wide mid-IR supercontinuum generation in As2S3 photonic crystal fiber by rods filling technique, Optik 158 (2018) 142–151, https://doi.org/10.1016/j.ijleo.2017.12.014.
[36] P. Chauhan, A. Kumar, Y. Kalra, Mid-infrared broadband supercontinuum generation in a highly nonlinear rectangular core chalcogenide photonic crystal fiber, Opt. Fiber Technol. 46 (2018) 174–178, https://doi.org/10.1016/j.yofte.2018.10.004.
[37] A. Medjouria, D. Abedb, Design and modelling of all-normal dispersion As39Se61 chalcogenide photonic crystal fiber for flat-top coherent mid-infrared supercontinuum generation, Opt. Fiber Technol. 50 (2019) 154–164, https://doi.org/10.1016/j.yofte.2019.03.021.
[38] A. Medjouria, D. Abedb, Z. Becera, Numerical investigation of a broadband coherent supercontinuum generation in Ga8Sb32S60 chalcogenide photonic crystal fiber with all-normal dispersion, Opto-Electron. Rev. 27 (1) (2019) 1–9, https://doi.org/10.1016/j.opelre.2019.01.003.
[39] A. Medjouri, D. Abed, Mid-infrared broadband ultraflat-top supercontinuum generation in dispersion engineered Ge-Sb-Se chalcogenide photonic crystal fiber, Opt. Mater. 97 (2019), 109391, https://doi.org/10.1016/j.optmat.2019.109391.
[40] P. Chauhan, A. Kumar, Y. Kalra, Numerical exploration of coherent supercontinuum generation in multicomponent GeSe2-As2Se3-PbSe chalcogenide based photonic crystal fiber, Opt. Fiber Technol. 54 (2020), 102100, https://doi.org/10.1016/j.yofte.2019.102100.
[41] H.P.T. Nguyen, T.H. Tuan, L. Xing, M. Matsumoto, G. Sakai, T. Suzuki, Y. Ohishi, Supercontinuum generation in a chalcogenide all-solid hybrid microstructured optical fiber, Opt. Express 28 (12) (2020) 17539–17555, https://doi.org/10.1364/OE.394968.
[42] E. Genier, P. Bowen, T. Sylvestre, J.M. Dudley, P. Moselund, O. Bang, Amplitude noise and coherence degradation of femtosecond supercontinuum generation in all-normal-dispersion fibers, J. Opt. Soc. Am. B 36 (2) (2019) A161–A167, https://doi.org/10.1364/JOSAB.36.00A161.
[43] T. Cheng, K. Nagasaka, T.H. Tuan, X. Xue, M. Matsumoto, H. Tezuka, T. Suzuki, Y. Ohishi, Mid-infrared supercontinuum generation spanning 2.0 to 15.1 μm in a chalcogenide step-index fiber, Opt. Lett. 41 (9) (2016) 2117–2120, https://doi.org/10.1364/OL.41.002117.
[44] B. Ung, M. Skorobogatiy, Chalcogenide microporous fibers for linear and nonlinear applications in the mid-infrared, Opt. Express 18 (8) (2010) 8647–8659, https://doi.org/10.1364/OE.18.008647.
[45] ⟨https://www.lumerical.com/products/mode/⟩.
[46] J.M. Dudley, J.R. Taylor, Supercontinuum Generation in Optical Fibers, first ed, Cambridge University Press, Cambridge, 2010, https://doi.org/10.1017/CBO9780511750465.
[47] G. Agrawal, Nonlinear Fiber Optics, sixth ed, Academic, Elsevier, 2019.
[48] L. Liu, T. Cheng, K. Nagasaka, H. Tong, G. Qin, T. Suzuki, Y. Ohishi, Coherent mid-infrared supercontinuum generation in all-solid chalcogenide microstructured fibers with all-normal dispersion, Opt. Lett. 41 (2) (2016) 392–395, https://doi.org/10.1364/OL.41.000392.
[49] A.M. Heidt, J.S. Feehan, J.H.V. Price, T. Feurer, Limits of coherent supercontinuum generation in normal dispersion fibers, J. Opt. Soc. Am. B 34 (2017) 764–775, https://doi.org/10.1364/JOSAB.34.000764.
[50] I. Kubat, O. Bang, Multimode supercontinuum generation in chalcogenide glass fibres, Opt. Express 24 (3) (2016) 2513–2526, https://doi.org/10.1364/OE.24.002513.
[51] I.B. Gonzalo, R.D. Engelsholm, M.P. Sørensen, O. Bang, Polarization noise places severe constraints on coherence of all-normal dispersion femtosecond supercontinuum generation, Sci. Rep. 8 (1) (2018) 1–13, https://doi.org/10.1038/s41598-018-24691-7.